

High redshift FR II radio galaxies: X-ray properties of the cores

E. Belsole^{1*}, D. M. Worrall¹ and M.J. Hardcastle²

¹ *Department of Physics, University of Bristol, Tyndall Avenue, Bristol BS8 1TL, UK*

² *School of Physics, Astronomy and Mathematics, University of Hertfordshire, College Lane, Hatfield, Hertfordshire AL10 9AB*

Accepted . Received ; in original form

ABSTRACT

We present an extensive X-ray spectral analysis of the cores of 19 FR II sources in the redshift range $0.5 < z < 1.0$ which were selected to be matched in isotropic radio power. The sample consists of 10 radio galaxies and 9 quasars. We compare our results with the expectations from a unification model that ascribes the difference between these two types of sources to the viewing angle to the line of sight, beaming and the presence of a dust and gas torus. We find that the spectrum of all the quasars can be fitted with a single power law, and that the spectral index flattens with decreasing angle to the line of sight. We interpret this as the effect of increasingly dominant inverse Compton X-ray emission, beamed such that the jet emission outshines other core components. For up to 70 per cent of the radio galaxies we detect intrinsic absorption; their core spectra are best fitted with an unabsorbed steep power law of average spectral index $\Gamma = 2.1$ and an absorbed power law of spectral index $\Gamma = 1.6$, which is flatter than that observed for radio-quiet quasars. We further conclude that the presence of a jet affects the spectral properties of absorbed nuclear emission in AGN. In radio galaxies, any steep-spectrum component of nuclear X-ray emission, similar to that seen in radio-quiet quasars, must be masked by a jet or by jet-related emission.

Key words: galaxies: active: high redshift: nuclei; quasars: general; radio continuum: galaxies; X-ray: galaxies

1 INTRODUCTION

Active Galactic Nuclei (AGN) are observed across the whole electromagnetic spectrum, but X-ray observations probe the process of converting gravitational energy into radiation most directly, as spectral and variability studies have shown that at least some of the X-ray emission comes from regions very close to the central engine. The most luminous AGN are found at high redshift and thus their study probes accretion processes and AGN environment early in the Universe.

AGN comprise a large variety of objects, for which both simple and more complicated classification schemes have been proposed. Unification Models explain the observed differences among AGN as the result of orientation with respect to the line of sight (e.g. Barthel 1989; Urry & Padovani 1995). In particular, it is proposed that powerful radio galaxies and radio-loud quasars are the same objects, and an obscuring torus is invoked to hide the nucleus of objects (namely radio galaxies) viewed at large angles to the jet axis (e.g. Barthel 1989).

Large orientation-unbiased samples of AGN are needed to test unification. They must be observed at many wavelengths, in order to detect both isotropic and anisotropic emission. At low radio frequencies optically-thin synchrotron radiation from the radio lobes

of radio-loud AGN dominates the emission, and this lobe emission should be isotropic. Thus, selection of objects via their low-frequency radio emission represents the most reliable method for selecting an orientation-unbiased sample. The low-frequency radio emission is also an indirect measure of the power supplied by the jet over the lifetime of the source (some 10^8 yr).

X-ray emission on small spatial scales, particularly at soft energies, is expected to be anisotropic because of the obscuring torus required in unified models to obscure the broad-line region and optical continuum emission. For those sources which are radio-loud, high-frequency nuclear radio emission, probing sub-arcsecond scales of the source, is explained as synchrotron radiation from the unresolved bases of relativistic jets, which is anisotropic due to relativistic beaming. The correlation found using *ROSAT* data between the nuclear, soft X-ray emission and the core radio emission of powerful radio-loud AGN (e.g. Hardcastle & Worrall 1999, Brinkmann et al. 1997) thus implies that at least part of the soft X-ray emission is also relativistically beamed and originates at the base of the jet (Hardcastle & Worrall 1999). From *ROSAT* data it had earlier been found that lobe-dominated quasars tend to lie above the flux-flux correlation valid for core-dominated quasars (Worrall et al. 1994), supporting the idea that lobe-dominated quasars are viewed at an angle to the line of sight such that the observer sees in X-ray both the jet-dominated component and a more isotropically emitted, probably nucleus-related component, with the two components being more similar in

* E-mail: e.belsole@bristol.ac.uk

flux density than for the core-dominated quasars. This suggestion is further supported by the rather flat X-ray spectra of radio-loud (core-dominated or blazar-type) quasars, with slopes $\Gamma \sim 1.5 - 1.6$ (e.g., Worrall & Wilkes 1990; Brinkmann, Yuan & Siebert 1997; Reeves et al. 1997; Reeves & Turner 2000; Gambill et al. 2003), which may be compared to the values of $\Gamma \sim 2$ more commonly found in their radio-quiet counterparts (e.g., Yuan et al. 1998; Reeves et al. 1997; Reeves & Turner 2000). The flat spectrum has been interpreted as the result of beamed emission from the jet.

X-ray results supporting unification of quasars with powerful, (narrow-line) radio galaxies (i.e. that those sources are viewed on the plane of the sky and are thus strongly obscured by a torus), especially at redshift above 0.5, are less abundant. Few such radio galaxies were detected in X-ray with *ROSAT*. However, Worrall et al. (1994) found that the core soft X-ray emission of the galaxy 3C 280 lies on an extrapolation of the correlation obtained for core-dominated quasars, and interpreted the result as due to X-ray emission from a jet-related component, with the nucleus-related component being obscured by a putative torus. This result was later extended to a larger sample of radio galaxies by Hardcastle & Worrall (1999).

In the simple picture of an obscuring torus, quasar light heats the gas and dust of the torus and thermal radiation is re-emitted isotropically in the mid/far-infrared in order to maintain energy balance in the inner regions. Thus, in principle, far-infrared radiation should provide an orientation-independent measure of the emitted power from the central engine. Studies based on data from *IRAS* (Heckman, Chambers & Postman 1992; Hes, Barthel & Hoekstra 1995), and later the Infrared Space Observatory (*ISO*) (e.g. Meisenheimer et al. 2001) were controversial because of the limited sensitivity and spectral coverage that made it difficult to separate star formation heating and AGN heating. The sensitivity in the mid/far-infrared of the *Spitzer* satellite provides for the first time the possibility to test this hypothesis for a large number of objects. Shi et al. (2005) have found that indeed AGN heating contributes more than 50 per cent of the far-infrared luminosity in most objects from a sample of 20 radio-loud galaxies and quasars.

A study of a sample of sources at a range of orientations for which X-ray and mid/far-infrared properties derived from high-quality data can be compared, is useful for understanding selection effects in X-ray-selected samples and for comparison with the new understanding of these sources coming from *Spitzer* data. Here we present high-quality X-ray observations obtained with *Chandra* and *XMM-Newton* of 19 sources in the redshift range $0.5 < z < 1.0$, which are mostly part of a larger sample of Fanaroff-Riley type II (FR II) radio galaxies and quasars currently being observed with *Spitzer*. In this paper we focus on the X-ray properties of the nuclear regions; we will address the environment of these sources (which is also a potential source of isotropic X-ray emission) in a forthcoming paper.

Throughout this paper we use the concordance cosmology with $h_0 = H_0/100 \text{ km s}^{-1} \text{ Mpc}^{-1} = 0.7$, $\Omega_M = 0.3$, $\Omega_\Lambda = 0.7$. If not otherwise stated, errors are quoted at 1σ for one interesting parameter.

2 THE SAMPLE

The AGN for our study were chosen from an orientation-unbiased parent sample. As discussed above, a reliable method for such a criterion is selection on the basis of the low-frequency radio emis-

sion. The best known and best studied orientation-unbiased sample of radio sources is the 3CRR sample (Laing, Riley, & Longair 1983), selected at 178 MHz. There are 50 3CRR sources at redshift $0.5 < z < 1.0$, of which $\sim 2/3$ are radio galaxies and $\sim 1/3$ are quasars. We do not aim to carry out a statistical test of unification models, for which a random selection from the parent sample would be necessary. Instead we intend to look for differences in the X-ray emitting components between quasars and radio galaxies, as would be expected in unification schemes. For this reason we base our work on a sub-sample of 34 high-redshift 3CRR radio galaxies and quasars that are being observed with *Spitzer* as part of a guaranteed-time programme.

These 34 sources were selected from the 3CRR on the basis of Galactic latitude for convenient scheduling of *Spitzer* observations, and they display similar distributions in redshift and isotropic radio power to the parent sample. Here we present X-ray results for 15 of the sources in this sample, those so far observed with *Chandra* or *XMM-Newton*. 3C 200 is part of the *Spitzer* sample although the source lies slightly outside the $0.5 < z < 1$ range, since *Chandra* observations were available at the time of the selection of the infrared sample. In addition, we have added to our study four sources (3C 228, 3C 265, 3C 345, 3C 454.3) that are not in the *Spitzer* sample, since they are in the same redshift range and have available high-quality X-ray observations. This gives us a sample of 19 sources (see Table 1). Figure 1 shows that for the quasars and radio galaxies in this subsample, the redshift, isotropic radio power, and radio flux distributions are similar.

Chandra or *XMM-Newton* observations of 9 sources (3C 184, 3C 200, 3C 220.1, 3C 228, 3C 263, 3C 275.1, 3C 292, 3C 330, 3C 334) were awarded to us in support of various projects, while data for the remaining sources were extracted from the *Chandra* archive. Table 1 lists the sources used in this work.

3 X-RAY OBSERVATIONS AND DATA PREPARATION

Table 2 lists basic observational information for the sources analysed in this paper. All *Chandra* observations were performed with ACIS-S with the source at the aimpoint of the S3 chip. For some bright sources (see Table 2) sub-array modes were used to reduce the readout time and hence the effect of pileup. The *XMM-Newton* observations for two sources, 3C 184 and 3C 292, discussed in this paper were taken with the EPIC cameras. Data analysis for these sources is described in Belsole et al. (2004).

Chandra data were processed using CIAO 3.2.1 and CALDB v3.0.2. We first removed the *afterglow* correction, and produced a new Level 1 event list. We then generated new bad-pixel files using the CIAO tool `ACIS_RUN_HOTPIX`. The new Level 1 photon lists were then processed using the CIAO tool `ACIS_PROCESS_EVENTS` in the standard way. The standard Charge Transfer Inefficiency (CTI) correction was not applied for 3C 220.1, since the focal plane temperature was higher than -120°C . For those observations telemetered in VFaint mode, we applied the additional background screening recommended for this mode, although this is not particularly useful for the study of the bright central component. We filtered for good grades (0, 2, 3, 4, 6) and generated a Level 2 photon list after filtering using the pipeline good-time-interval (GTI) filter. Finally, for each source we produced a light curve in a region void of sources to check for variability of the background. No strong flare events were found in any of our sources. However, all data sets were filtered following the prescription given in <http://asc.harvard.edu/ciao/threads/filter/>.

Table 1. The sample

Source	RA(J2000) h m s	Dec(J2000) ° ' "	redshift	scale kpc/arcsec	type	N_{H} 10^{20} cm^{-2}	Comments
3C 6.1	00 16 30.99	+79 16 50.88	0.840	7.63	NLRG	14.80	
3C 184	07 39 24.31	+70 23 10.74	0.994	8.00	NLRG	3.45	
3C 200	08 27 25.44	+29 18 46.51	0.458	5.82	NLRG	3.74	
3C 207	08 40 47.58	+13 12 23.37	0.684	7.08	QSO	4.12	
3C 220.1	09 32 39.65	+79 06 31.53	0.610	6.73	NLRG	1.87	
3C 228	09 50 10.70	+14 20 00.07	0.552	6.42	NLRG	3.18	no <i>Spitzer</i>
3C 254	11 14 38.71	+40 37 20.29	0.734	7.28	QSO	1.90	
3C 263	11 39 57.03	+65 47 49.47	0.646	6.90	QSO	1.18	
3C 265	11 45 28.99	+31 33 49.43	0.811	7.54	NLRG	1.90	no <i>Spitzer</i>
3C 275.1	12 43 57.67	+16 22 53.22	0.557	6.40	QSO	1.99	
3C 280	12 56 57.85	+47 20 20.30	0.996	8.00	NLRG	1.13	
3C 292	13 50 41.95	+64 29 35.40	0.713	6.90	NLRG	2.17	
3C 309.1	14 59 07.60	+71 40 19.89	0.904	7.80	GPS-QSO	2.30	
3C 330	16 09 34.71	+65 56 37.40	0.549	6.41	NLRG	2.81	
3C 334	16 20 21.85	+17 36 23.12	0.555	6.38	QSO	4.24	
3C 345	16 42 58.80	+39 48 36.85	0.594	6.66	core-dom QSO	1.13	no <i>Spitzer</i>
3C 380	18 29 31.78	+48 44 46.45	0.691	7.11	core-dom QSO	5.67	
3C 427.1	21 04 06.38	+76 33 11.59	0.572	6.49	LERG	10.90	
3C 454.3	22 53 57.76	+16 08 53.72	0.859	7.68	core-dom QSO	6.50	no <i>Spitzer</i>

Galactic column density is from Dickey & Lockman (1990); NLRG means Narrow Line Radio Galaxy; LERG means low-excitation radio galaxy. Redshifts and positions are taken from Laing et al. (1983).

Table 2. Observation log. Col 1: 3CRR name; Col. 2: Instrument used for the observations, C stands for *Chandra*, X for *XMM-Newton*; Col.3: Observation ID; Col. 4: Date of observation; Col 5: Detector, where the numbers following “ACIS” correspond to the CCD chips turned on during observation. The target was placed at the aim point of chip 7. EPIC means that MOS and pn cameras have been used for the observation and analysis; 3C 184 was observed with MOS cameras only for observation ID 0028540201; Col. 6: Observation mode. For *XMM-Newton* observations the filter is also listed and the mode refers to the EPN camera; Col. 7: Frame readout time; the first value for *XMM-Newton* observations refers to MOS cameras; Col. 8: Nominal exposure Time; Col.9: Net exposure time, after flare screening; Col. 10: Pileup fraction.

Source	Instrument	Obs ID	Obs Date	Detector	MODE	TIME/FRAME sec	EXPOSURE ks	Screened time ks	Pileup fraction
3C 6.1	C	4363	2002-08-26	ACIS-235678	VFAINT	3.24	20	20.0	5%
	C	3009	2002-10-15	ACIS-235678	VFAINT	3.24	36	35.7	5%
3C 184	C	3226	2002-09-22	ACIS-23678	VFAINT	3.14	20	18.9	1%
	X	0028540201	2001-09-19	EPIC/MOS	Thin/FF	2.6	38.9	32/-	na
	X	0028540601	2002-03-10	EPIC	Thin/EFF	2.6/0.2(pn)	40.9	26/16.4(pn)	na
3C 200	C	838	2000-10-06	ACIS-235678	FAINT	3.24	16	14.7	1%
3C 207	C	2130	2000-11-04	ACIS-235678	FAINT	3.24	39	37.5	22%
3C 220.1	C	839	1999-12-29	ACIS-23678	FAINT	3.24	21	18.5	7%
3C 228	C	2453	2001-04-23	ACIS-235678	FAINT	3.24	12	10.6	2%
	C	2095	2001-06-03	ACIS-235678	FAINT	3.24	15.5	13.8	3%
3C 254	C	2209	2001-03-26	ACIS-23678	VFAINT	3.14	31	29.5	20%
3C 263	C	2126	2000-10-28	ACIS-235678	FAINT	3.24	51	48.8	26%
3C 265	C	2984	2002-04-25	ACIS-235678	VFAINT	3.24	59	50.6	1%
3C 275.1	C	2096	2001-06-02	ACIS-567	FAINT	1.64	26	24.8	4%
3C 280	C	2210	2001-08-27	ACIS-235678	VFAINT	3.24	63.5	46.3	< 1%
3C 292	X	0147540101	2002-10-29	EPIC	Medium/FF	2.6/0.07(pn)	33.9	20/17(pn)	< 1%
3C 309.1	C	3105	2002-01-28	ACIS-7	VFAINT	0.44	17	16.6	6%
3C 330	C	2127	2001-10-16	ACIS-235678	FAINT	3.24	44	43.8	0%
3C 334	C	2097	2001-08-22	ACIS-567	FAINT	0.94	33	30.2	9%
3C 345	C	2143	2001-04-27	ACIS-7	FAINT	0.44	10	9.0	13%
3C 380	C	3124	2002-05-20	ACIS-7	FAINT	0.84	5.5	5.3	16%
3C 427.1	C	2194	2002-01-27	ACIS-235678	FAINT	3.24	39	39.0	0%
3C 454.3	C	3127	2002-11-06	ACIS-7	FAINT	0.84	5.5	5.5	24%

We then applied an astrometry correction to the final event list using the tool available on line¹. The level 2 event lists were then used for the analysis described below.

4 ANALYSIS

4.1 Spatial analysis

We performed preliminary spatial analysis on the *Chandra* data in order to investigate whether the X-ray radial profile was consistent with the instrumental point spread function (PSF). PSFs for each

¹ http://asc.harvard.edu/cal/ASPECT/fix_offset/fix_offset.cgi

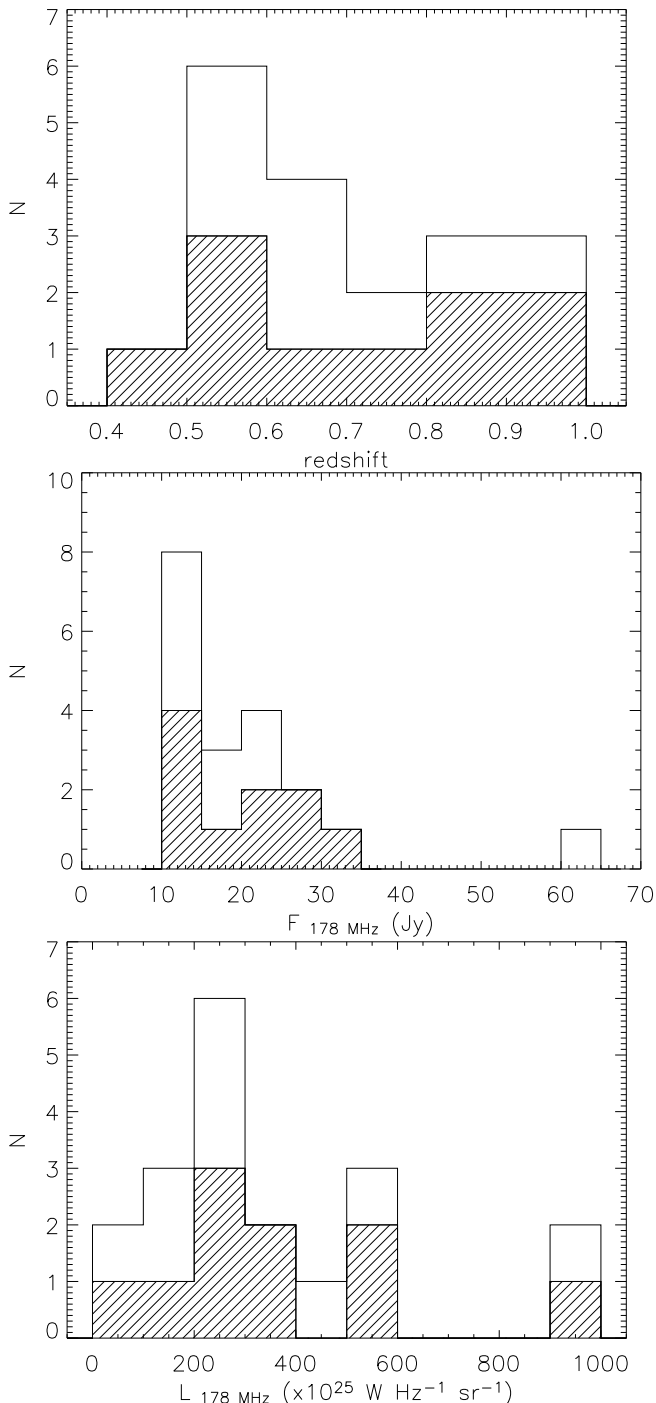


Figure 1. Redshift (Top), isotropic (178 MHz) radio flux (Middle) and power (bottom) for the sample of 19 sources analysed in this paper. The shaded area corresponds to the 10 radio galaxies.

source were generated using the PSF library for ACIS at a convenient energy depending on the spectrum of the source. For most sources this was 2.5 keV. We then used the CIAO tool MKPSF to simulate a point source image, and the tool DMIMGCALC to normalize the PSF to the count rate of each source. We extracted radial profiles for each source in the energy range 0.5-8.0 keV and compared with the radial profile derived for the simulated PSF. Features such as jet emission or extended emission clearly associated with the radio lobes were masked prior to the radial profile extraction.

We are aware that this approach is not perfect since a monochromatic estimate of the PSF was used. However, it gives an estimate of the extent of the PSF that is good enough to allow us to define the radius for spectral analysis of the nuclear region and the associated background for each source, especially in cases where the sources are piled up.

This quick spatial analysis also gives indications of the presence of extended emission associated with a cluster-like environment or inverse-Compton scattering in the radio lobes (Croston et al. 2005). We will discuss the environments of these sources in a future paper.

We found that for most of the sources more than 90 per cent of the flux was included in a circular region of radius 2.5 pixels. The radial profile of 3C 200 shows that extended emission starts to dominate at ~ 2 arcsec from the X-ray peak. However, only 2 counts contribute to the extended flux in the circular region used for the spectral analysis, and this is much less than any statistical error. For 3C 263 we found that the point source photon distribution was broader than the PSF obtained at 2.5 keV, which is likely to be the effect of the strong pileup (see Sect. 4.3): a piled-up point source will show a photon distribution which is flatter in the centre and broader in the wings than a standard PSF as calculated with MKPSF. For all sources, we applied corrections for the missing fraction of the PSF (see below) to the X-ray fluxes we quote.

4.2 Timing analysis

For all *Chandra* observations we generated light curves from the 0.5-8.0 keV energy range for each core using the CIAO tool DMEXTRACT, and in different time bins from 100 to 4000 s intervals, depending on the source exposure time and photon statistics (we did not perform timing analysis for the *XMM-Newton* observation of 3C 292).

We used χ^2 to test for significant deviations from the average count rate within the light curve, and Table 3 reports these χ^2 values calculated using the binning that shows the largest deviation from a constant value as well as the probability that the light curve is constant. None of our sources exhibits significant time variability, including 3C 207 (Hough et al. 2001), and the core-dominated quasars which are known to be variable at 5 GHz (and higher frequency) on time scales of years (e.g., Lister, Tingay & Preston 2001; Aller, Aller & Hughes 2003). 3C345 in particular was found to be variable in X-ray flux density (Unwin et al. 1997), but on timescales of order of weeks.

We investigated flux variability for the two sources which were observed in two exposures, 3C 6.1 and 3C 228. The average count rate for the two exposures of 3C 6.1 are $0.044 \pm 0.008 \text{ s}^{-1}$ and $0.039 \pm 0.014 \text{ s}^{-1}$ for exposure IDs 3009 and 4363, respectively. 3C 228 does not show any flux variability either, with both exposures having count rate of $0.023 \pm 0.005 \text{ s}^{-1}$.

4.3 X-ray spectral fitting

The spectrum of each core was extracted from a circle of radius 2.5 pixels (1.23 arcsec; core region), which includes > 90 per cent of the ACIS-S3 PSF (as verified by our spatial analysis). A local background region was selected from an annulus of internal and external radii 3.5 and 6 pixels. This choice of background should provide the best possible subtraction of any contribution from a cluster-like environment. In all cases the core strongly dominates any such extended emission. The net counts in the core region in

Table 3. X-ray variability

Source	time bin s	$\chi^2_r/\text{d.o.f.}$	P_{χ^2}
3C 6.1/3009	750	0.599/27	0.950
3C 6.1/4363	2000	0.663/18	0.850
3C 184	3000	0.450/6	0.846
3C 200	2000	0.650/7	0.715
3C 207	1000	0.521/38	0.993
3C 220.1	650	0.806/30	0.764
3C 228/2095	3000	1.012/5	0.962
3C 228/2453	2000	0.600/5	0.700
3C 254	3000	0.568/10	0.842
3C 263	500	0.470/100	1.000
3C 265	3000	0.648/17	0.856
3C 275.1	750	38.549/10	0.000
3C 280	3000	0.500/14	0.935
3C 309.1	3000	0.612/6	0.721
3C 330	3000	0.464/15	0.959
3C 334	2000	0.496/17	0.956
3C 345	750	13.305/14	0.503
3C 380	650	1.286/9	0.238
3C 427.1	4000	0.300/9	0.975
3C 454.3	1000	0.711/5	0.615

Numbers given after multiple observations of the same source are the *Chandra* observation IDs. The time bin is the one that gives the largest χ^2 value (see the text). The probability P_{χ^2} is the probability of obtaining a value of χ^2 as extreme as this under the null hypothesis of no variability.

the 0.2–10.0 keV energy band, for each source, are listed in Table 4.

Spectra were extracted using the tool PSEXTRACT, which generates Ancillary Response Files (ARF) and Redistribution Matrix Files (RMF). Spectra were grouped to have a minimum of 15 to 20 counts per channel (except for the *Chandra* observations of 3C 184 and 3C 427.1 where there are too few counts for spectral fitting). We used version 3.0.2 of the calibration database, which accounts for spatial variation of the Quantum Efficiency (QE) degradation.

Because of the nature of the sources discussed here, the issue of pileup needed to be considered. Pileup will distort the spectrum at high energy (for details see Ballet 1999; Davis 2001). An indication of the pileup fraction (PUF; defined as the ratio of the number of detected events that consist of more than one photon to the total number of detected events) was estimated using PIMMS and Figure 6.18 in the *Chandra* Proposers’ Observatory Guide Sect. 6.14². The PUF was calculated for each source, and is listed in Table 2. Pileup effects were ignored if the PUF was less than 8 per cent, although we verified that the addition of a pileup model in XSPEC did not change the best-fit parameters for such sources (see Sect. 5.1 for more details). For those sources for which a higher PUF was found, we excluded a circle of radius from 1 to 2 pixels (see below for details of each individual source) from the initial circle of radius 2.5 pixels and used this annulus as the region for spectral analysis, since the wings of the PSF are less affected by pileup. Although an annular region contains only a fraction of the PSF, it is valuable in finding the correct spectral index of the source. To measure fluxes and flux densities for these sources we adjusted the normalization

to account for missing counts based on simulating the PSF at the position of the source using MARX. Although this correction is dependent on the source spectrum, it has been shown that for NGC 6251 the spectral dependence is negligible (Evans et al. 2005). We applied similar tests to those applied for NCG 6251 to 3C 334, and found that any correction due to the energy-dependence of the PSF is within the statistical errors. Therefore we ignored energy dependence when correcting fluxes and flux densities for the missing PSF, and we corrected solely for the fraction of the PSF missing at the energy of 2.5 keV.

In the case of 3C 263, which is heavily piled-up, we adopted the spectrum extracted in an annulus of inner and outer radii 3 and 5 pixels, after inspecting the radial profile.

Spectral analysis was performed using XSPEC v11.3.1. All spectra were fitted in the energy band 0.5–8.0 keV, where the ACIS-S calibration is most precise. We initially fitted the background-subtracted core spectrum with a model composed of Galactic absorption (see Table 1), and a power law. Additional components were added to the model as required after inspection of the residuals. The significance of adding additional model components to the fit was estimated using the F -test.

Fluxes, flux densities and luminosities for all sources whose spectrum was extracted in the canonical circle of radius 2.5 pixels were corrected by 10 per cent to account for the missing PSF fraction. Values derived from spectra extracted in annular regions were corrected appropriately as described above. Moreover, as a conservative approach, we added a 10 per cent systematic error to the error estimates for the fluxes, flux densities and luminosities of all sources with pileup fraction greater than 8 per cent (see Table 2).

5 RESULTS

5.1 X-ray spectral properties

The results of the spectral fitting are reported in Table 4. A single power law absorbed by Galactic absorption provides a good fit to the core continuum for 11 sources (3C 200, 3C 207, 3C 220.1, 3C 228, 3C 254, 3C 263, 3C 275.1, 3C 309.1, 3C 334, 3C 380, 3C 434.3), of which 8 are lobe-dominated or core-dominated quasars. Intrinsic absorption is required for 7 sources, all of them radio galaxies (3C 6.1, 3C 184, 3C 265, 3C 280, 3C 292, 3C 330, 3C 427.1). An additional thermal component is required for only 1 object, 3C 184, a very small radio source observed with *XMM-Newton* for which cluster-scale X-ray emission was detected (Belsole et al. 2004). This is much less than any statistical error. In only one case, 3C 345, is a single power law not an acceptable fit for a quasar. A second power law is necessary to account for the flattening above 1.7 keV in the core spectrum. This is in agreement with the results of Gambill et al. (2003), who used a broken power law to fit the spectrum. Several of the radio galaxies required a soft unabsorbed power law in addition to the absorbed power law. Details of additional continuum components, both non-thermal and thermal, required to fit the core spectra of the sources in our sample are listed in Table 5.

In agreement with Bondi et al. (2004), we detect significant line emission for 3C 265, indicating a neutral Fe line at a rest-frame energy of 6.37 ± 0.13 keV and of equivalent width 443^{+196}_{-190} eV. The core spectrum of 3C 330 displays a broad, asymmetric line at rest-frame energy $6.7^{+0.6}_{-0.3}$ keV. Although this may suggest the presence of ionized iron in the central region, deeper observations of this source are needed to establish the reality of the line.

² <http://asc.harvard.edu/proposer/POG/html/ACIS.html>
#SECTION03714000000000000000

Table 4. Spectral fit results for the core region. **Col. 1:** source 3CRR name; **Col. 2:** net counts in the 0.2–10.0 keV energy band contained in a circular region of radius 2.5 pixels; if two exposures have been used this is the sum of the two data sets; **Col. 3:** intrinsic N_{H} , when required; **Col. 4:** power law index. This corresponds to the slope of the hard spectrum when a composite model is used; **Col. 5:** normalization of the power law model, in units of photons $\text{keV}^{-1} \text{cm}^{-2} \text{s}^{-1}$ at 1 keV. The normalization corresponds to the best-fit value found while fitting the region specified in Col. 9 and does not correspond to the final luminosity displayed in Col. 8. Moreover, the normalization corresponds to the power law used to fit the hard spectrum when a model composed of more than one power-law is adopted; **Col. 6:** $\chi^2/\text{d.o.f.}$ corresponding to the best-fitting model; **Col. 7:** where the best-fitting model was not a power law with Galactic absorption, this column gives the probability under the null hypothesis (from the F -test) of obtaining an improvement in χ^2 as large as was observed. When not applicable the original model represents a good fit to the data; **Col. 8:** unabsorbed X-ray Luminosity in the energy band 2.0–10.0 keV - absorbed component only in radio galaxies (flux for the same component is listed in Table 6); **Col. 9:** comments; if there are no comments, the region used for spectral analysis is a circle of radius 2.5 pixels.

Source	net counts [0.2-10 keV]	N_{H} (intrinsic) $\times 10^{22} \text{ cm}^{-2}$	Gamma	Norm $\times 10^{-5}$ (ph/keV/cm/s)	$\chi^2/\text{d.o.f.}$	F -test	L_{X} [2-10 keV] $\times 10^{44}$ (erg s $^{-1}$)	Comments
3C 6.1	2326±49	0.28 $^{+0.11}_{-0.10}$	1.53 $^{+0.06}_{-0.07}$	6.5 $^{+0.4}_{-0.5}$	139.1/126	3.6×10 $^{-3}$	10.0 $^{+0.7}_{-0.6}$	2 exposures combined
3C 184 ^a	776±65	48.7 $^{+22.0}_{-12.1}$	1.4 $^{+0.3}_{-0.2}$	2.4 $^{+1.1}_{-1.0}$	39.3/44	2.7×10 $^{-7}$	5.7 $^{+2.2}_{-2.0}$	XMM
3C 200	166±14	na	1.68 $^{+0.18}_{-0.16}$	1.3 $^{+0.1}_{-0.2}$	5.3/5	na	0.41 $^{+0.07}_{-0.08}$	
3C 207	6349±80	na	1.27 $^{+0.05}_{-0.05}$	3.6 $^{+0.1}_{-0.1}$	96.5/105	na	13.7 $^{+1.7}_{-2.1}$	1.0-2.5 pix annulus
3C 220.1	1133±34	na	1.55 $^{+0.04}_{-0.05}$	5.4 $^{+0.2}_{-0.2}$	55.3/57	na	3.9 $^{+0.2}_{-0.1}$	
3C 228	646±50	na	1.59 $^{+0.11}_{-0.10}$	2.7 $^{+0.2}_{-0.2}$	23.7/32	na	1.5 $^{+0.1}_{-0.1}$	2 exposures combined
3C 254	4528±70	na	1.64 $^{+0.11}_{-0.10}$	1.4 $^{+0.2}_{-0.1}$	34.1/33	na	20.8 $^{+4.4}_{-3.1}$	1.5-2.5 pix annulus
3C 263	9759±100	na	1.88 $^{+0.10}_{-0.10}$	1.10 $^{+0.08}_{-0.04}$	14.2/20	na	15.0 $^{+2.5}_{-1.9}$	2.5-5.0 pix annulus
3C 265	285±17	16.8 $^{+10.5}_{-7.2}$	1.01 $^{+0.66}_{-0.30}$	1.3 $^{+2.5}_{-0.8}$	5.6/10	3.2×10 $^{-3}$	3.1 $^{+1.2}_{-1.2}$	
3C 275.1	1302±36	na	1.45 $^{+0.05}_{-0.05}$	5.1 $^{+0.2}_{-0.2}$	62.0/63	na	3.3 $^{+0.2}_{-0.1}$	
3C 280 ^c	53±8	9.7 $^{+6.2}_{-4.7}$	1.27 $^{+0.43}_{-0.41}$	0.4 $^{+0.1}_{-0.1}$	0.7/3	2.0×10 $^{-2}$	10.0 $^{+3.5}_{-3.5}$	
3C 292 ^b	251±10	26.4 $^{+12.8}_{-5.9}$	2.05 $^{+0.15}_{-0.15}$	4.5 $^{+1.8}_{-1.3}$	14.6/19	1.8×10 $^{-4}$	2.5 $^{+0.7}_{-0.7}$	XMM
3C 309.1	5528±75	na	1.54 $^{+0.02}_{-0.03}$	34.2 $^{+0.5}_{-0.7}$	159.4/169	na	60.0 $^{+2.0}_{-2.0}$	
3C 330	118±11	23.6 $^{+16.3}_{-13.4}$	1.95 $^{+0.55}_{-0.36}$	2.3 $^{+1.4}_{-1.8}$	6.7/6	1.3×10 $^{-1}$	0.8 $^{+0.2}_{-0.6}$	
3C 334	7241±85	na	1.74 $^{+0.04}_{-0.05}$	8.2 $^{+0.2}_{-0.3}$	105.4/78	na	12.0 $^{+2.2}_{-2.2}$	1.0-2.5 pix annulus
3C 345	6637±81	na	1.27 $^{+0.11}_{-0.11}$	15.8 $^{+2.3}_{-2.1}$	87.8/83	1.2×10 $^{-2}$	43.3 $^{+7.7}_{-5.0}$	1.0-2.5 pix annulus
3C 380	2553±51	na	1.54 $^{+0.09}_{-0.09}$	12.5 $^{+1.2}_{-1.0}$	15.5/20	na	65.0 $^{+12.5}_{-12.5}$	1.5-2.5 pix annulus
3C 427.1	15±3	10 (fix)	1.6 (fix)	0.2 $^{+0.1}_{-0.1}$	2.7 ^d	na	0.13 $^{+0.05}_{-0.05}$	C -statistics used
3C 454.3 ^f	3889±63	na	1.25 $^{+0.15}_{-0.15}$	5.3 $^{+0.7}_{-0.7}$	9.0/8	na	235.0 $^{+60.0}_{-60.0}$	2.0-2.5 pix annulus

Chandra data fits were done in the 0.5-8.0 keV band; “2 exposures” in Col. 9 means that the spectra from both exposures of the source have been used. Luminosities are corrected for the extraction aperture while normalizations are the actual, best-fit value. ^a Parameters are from *XMM-Newton* data fitting. The total spectrum of the source was extracted in a circle of radius 40 arcsec; the count rate in Col. 2 corresponds to the total EPIC count rate in this region (see Belsole et al. 2004 for details); the *Chandra* observation of 3C 184 contains 41 counts in the energy band [0.2-10.0] keV. The *XMM-Newton* and *Chandra* fitting results are in agreement, but the former was preferred since gives significantly better constraints. ^b The *XMM-Newton* core spectrum was extracted in a circular region of radius 10 arcsec, and the count rate is the total EPIC background-subtracted count rate in this region (the background estimated in an annulus of inner radius 30 arcsec and outer radius 35 arcsec – see Belsole et al. 2004 for details); the ARF accounts for the missing PSF, and the spectrum was fitted between 0.3 and 10 keV. ^c An F -test was performed for a model with intrinsic absorption versus a model with no intrinsic absorption; see the details for this source in Appendix A for discussion of an unabsorbed component at soft energies. ^d C -statistic value instead of χ^2 . The quoted error is the “real” error, i.e. statistical plus systematic.

Table 5. Spectral fit results for the core region: Additional components

Source	Soft PL		Thermal		Flux [0.2-10.0] keV (erg s $^{-1}$ cm $^{-2}$)	L_{X} (erg s $^{-1}$)
	Γ	N_{PL} $\times 10^{-5}$	kT (keV)	N_{Th} $\times 10^{-5}$		
3C 184 ^a	1.9 $^{+1.4}_{-1.5}$	0.1 $^{+0.2}_{-0.09}$	3.6 $^{+14.1}_{-1.8}$	2.3 $^{+0.5}_{-0.5}$	7.3 × 10 $^{-15}$	3.0 × 10 43
3C 265	2.1 $^{+0.8}_{-0.7}$	0.17 $^{+0.04}_{-0.04}$	—	—	1.0 × 10 $^{-14}$	2.8 × 10 43
3C 280	2.2(fix)	0.02 $^{+0.01}_{-0.01}$	—	—	1.5 × 10 $^{-15}$	7.1 × 10 42
3C 292	2.7 $^{+0.6}_{-0.7}$	0.2 $^{+0.1}_{-0.1}$	—	—	1.3 × 10 $^{-14}$	4.2 × 10 43
3C 330	1.9 $^{+0.8}_{-0.7}$	0.16 $^{+0.03}_{-0.03}$	—	—	1.0 × 10 $^{-14}$	1.2 × 10 43
3C 345	1.8 $^{+0.1}_{-0.1}$	21.3 $^{+0.6}_{-0.7}$	—	—	5.0 × 10 $^{-12}$	6.0 × 10 45
3C 427.1	2.2(fix)	< 0.08	—	—	< 4.5 × 10 $^{-15}$	< 5.6 × 10 42

Upper limits are quoted at the 3σ confidence level for one interesting parameter; errors are the 1σ confidence range. ^a Flux and luminosity refer to the soft power-law component. The soft power-law parameters were obtained by fitting the *Chandra* spectrum. The bolometric X-ray luminosity of the thermal component is $8.3 \times 10^{43} \text{ erg s}^{-1}$ (Belsole et al. 2004).

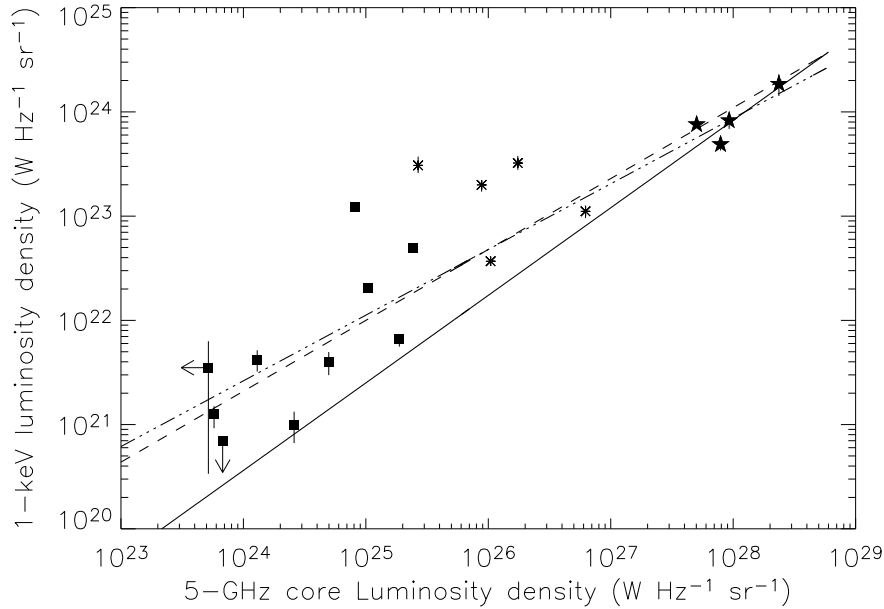


Figure 2. 1-keV X-ray core versus 5-GHz radio core spectral luminosity density. Symbols are as follows: filled squares are radio galaxies (when applicable only the unabsorbed component was taken into account to compute the 1-keV luminosity density); asterisks are lobe-dominated quasars and stars are core-dominated quasars. The dot-dashed line corresponds to the maximum likelihood linear regression method applied to the whole sample. The dashed line is the linear regression applied to the sample composed of core-dominated quasars and radio galaxies only. The continuous line corresponds to the best fit regression for core-dominated quasars only. When 1σ error bars are not visible they are smaller than the symbols.

Table 6. X-ray and radio fluxes and flux densities

Source	$f_{1\text{keV}}$ (nJy)	$L_{1\text{keV}} \times 10^{22}$ (W Hz $^{-1}$ sr $^{-1}$)	$f_{2.0-10.0\text{keV}}$ ($\times 10^{-13}$ erg cm $^{-2}$ s $^{-1}$)	core $f_{5\text{GHz}}$ (mJy)	core $L_{5\text{GHz}} \times 10^{24}$ (W Hz $^{-1}$ sr $^{-1}$)	total $L_{178\text{MHz}} \times 10^{25}$ (W Hz $^{-1}$ sr $^{-1}$)	α_R
3C 6.1	$47.6^{+2.9}_{-3.7}$	$12.18^{+0.74}_{-0.95}$	$3.9^{+0.5}_{-0.4}$	4.4	8.2	332	0.68
3C 184	$0.73^{+0.58}_{-0.66}$	$0.35^{+0.28}_{-0.32}$	$1.7^{+0.7}_{-0.6}$	<0.2	<0.5	535	0.86
3C 200	$9.5^{+0.8}_{-1.4}$	$0.66^{+0.06}_{-0.1}$	$0.6^{+0.1}_{-0.1}$	35.1	18.8	71.7	0.84
3C 207	79.1 ± 11	$11.11^{+1.55}_{-1.55}$	$9.7^{+1.3}_{-1.3}$	510 ^V	622.5	229	0.90
3C 220.1	$39.8^{+1.3}_{-1.4}$	$4.99^{+0.16}_{-0.18}$	$2.7^{+0.1}_{-0.1}$	25	24.1	210	0.93
3C 228	$19.8^{+2.0}_{-1.3}$	$2.02^{+0.20}_{-0.13}$	$1.4^{+0.1}_{-0.1}$	13.3	10.5	231	1.0
3C 254	$153.3^{+32.9}_{-24.1}$	$30.67^{+6.58}_{-4.82}$	$10.4^{+2.2}_{-1.4}$	19	26.7	412	0.96
3C 263	$187.2^{+32.0}_{-26.1}$	$32.31^{+5.52}_{-4.51}$	$9.0^{+1.2}_{-1.4}$	157	174.2	220	0.82
3C 265 ^a	$1.2^{+0.3}_{-0.3}$	$0.40^{+0.09}_{-0.10}$	$1.8^{+0.3}_{-0.5}$	2.9	5.0	515	0.96
3C 275.1	$37.6^{+1.4}_{-1.2}$	$3.69^{+0.14}_{-0.12}$	$3.4^{+0.1}_{-0.1}$	130 ^V	104.5	194	0.96
3C 280 ^a	$0.18^{+0.08}_{-0.09}$	$0.10^{+0.03}_{-0.03}$	$0.3^{+0.1}_{-0.1}$	1.0(7%)	2.6	931	0.81
3C 292 ^a	$1.3^{+0.3}_{-0.3}$	$0.42^{+0.09}_{-0.1}$	$1.1^{+0.2}_{-0.2}$	1.0(11%)	1.3	180	0.80
3C 309.1	$250.4^{+4.0}_{-5.3}$	$75.90^{+1.21}_{-1.60}$	$19.9^{+0.2}_{-0.3}$	2350	5030.0	591	0.53
3C 330	$1.1^{+0.2}_{-0.2}$	$0.13^{+0.02}_{-0.03}$	$0.7^{+0.2}_{-0.5}$	0.74(6%)	0.6	255	0.71
3C 334	$181.0^{+19.0}_{-25.0}$	$19.94^{+2.09}_{-2.75}$	$10.0^{+2.0}_{-2.0}$	111	88.2	110	0.86
3C 345	$470.4^{+62.5}_{-60.3}$	$48.89^{+6.49}_{-6.27}$	$46.0^{+7.6}_{-13.6}$	8610 ^V	7889.9	97.2	0.27
3C 380	$500.3^{+80.3}_{-84.5}$	$82.72.0^{+13.28}_{-13.97}$	$40.0^{+8.0}_{-8.0}$	7447	9272.1	930	0.71
3C 427.1	< 0.5	< 0.07	$0.1^{+0.04}_{-0.04}$	0.8(4%)	0.68	302	0.97
3C 454.3	820^{+192}_{-192}	$185.49^{+43.43}_{-23.63}$	$100^{+21.0}_{-14.0}$	12200 ^V	2.36×10^4	224	0.04

^a Flux density at 1 keV is computed by using the soft component only, upper limits when appropriate. The 2.0-10.0 keV flux is from the absorbed component only in the case of radio galaxies. ^V the source is known to be variable at the measured frequency. Errors are quoted at 1σ confidence for one interesting parameter; upper limits are 3σ confidence level. Unless otherwise stated, errors on the 5 GHz flux densities are 3%, as defined by calibration errors.

Hints of possible line emission are seen in 3C 207 (ionized, see also Brunetti et al. 2002) and 3C 275.1 (neutral), although the addition of a line does not technically improve these fits.

5.2 X-ray versus radio correlations

In Table 6 we list the unabsorbed X-ray flux density at 1 keV, derived from our spectral fitting, and the 5-GHz core flux density, obtained from various sources and tabulated in the on-line 3CRR

catalogue³. Errors on the radio measurements are generally dominated by the calibration errors (of order 3 per cent) and are thus small compared to the X-ray errors. Where the uncertainty is dominated by thermal noise we tabulate per-source uncertainties in Table 6. We have also computed the 1-keV and 5-GHz rest frame spectral luminosity densities, assuming $\alpha_X = \Gamma - 1$ where Γ is the best-fit spectral index. In general the spectral indices of the radio cores are not known (and likely to be variable) but as compact cores are known to have typical spectral indices close to 0 (e.g. Bridle & Fomalont 1978) we adopt $\alpha_R = 0$ in calculating the rest-frame radio luminosities. We used the analysis package ASURV Rev 1.1 (LaValley, Isobe & Feigelson 1992), to calculate the generalized Kendall's τ coefficient in the presence of censored data to the relation between core 1-keV flux density and the core 5 GHz flux density. We found that the flux-flux correlation is significant for the sample as a whole, as well as for subsamples of data. This support the idea that the luminosity-luminosity correlation is not redshift-induced. However, to test correlations between properties of sources spanning a wide redshift range, and particularly for high-redshift sources for which K -correction must be taken into account, the respective luminosity values should be used (e.g. Kembhavi et al. 1986). We apply the generalized Kendall's τ algorithm to the 1-keV luminosity density and 5-GHz luminosity density correlation (see Table 7). Linear regression were evaluated by applying a maximum-likelihood fitting routine to fit a model consisting of a straight line in log space and an intrinsic dispersion to the luminosities. Our fitting procedure takes into account the uncertainties and upper limits on the radio and X-ray data points and is intrinsically symmetrical with respect to the two types of luminosity. 90 per cent errors on the fitted slopes were estimated using a Monte Carlo method.

Logarithmic slopes for all subsamples are consistent within the errors, mainly because of the limited statistics. However, we observe a trend when taking the best fits at their face value (see Table 7, where we also list the intrinsic dispersion as 1-sigma values of Gaussians in log space). The slope of the best-fit correlation deviates significantly from 1 only when samples containing more than one class of object are fitted, and it becomes very close to 1 when samples consisting only of radio galaxies or core-dominated quasars are fitted (with a possible flattening for the latter, consistent with what was observed in larger samples of core-dominated quasars; e.g., Kembhavi, Feigelson & Singh 1986; Worrall et al. 1994).

The dot-dashed line in Figure 2 shows the linear regressions for the whole sample, while the dashed line shows the same regression to the sample composed of core-dominated quasars and radio galaxies. We also show the linear regressions found when fitting only core-dominated quasars (continuous line). We observe that lobe-dominated quasars (asterisks) lie above the correlation valid for core-dominated quasars (see. e.g., Worrall et al. 1994; Hardcastle & Worrall 1999). We also notice that 3 radio galaxies lie in the $L_X - L_R$ plane above *all* correlations, suggesting a behaviour similar to lobe-dominated quasars. However, this is not surprising since the radio galaxies in question are 3C 6.1, 3C 220.1 and 3C 228, for which a simple power-law spectral model is a good fit to the data. It is interesting that the radio galaxies have excess X-ray emission over an extrapolation from the core-dominated quasars, and may suggest a difference in the mechanisms responsible for the jet-related X-ray emission in the two class of objects.

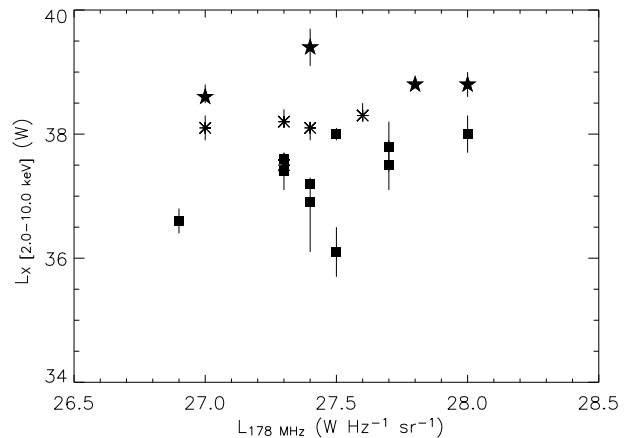


Figure 3. X-ray luminosity in the energy band 2.0-10.0 keV (using the unabsorbed luminosity of absorbed components in the radio galaxies) versus the 178 MHz luminosity density. Symbols are as follow: filled squares are radio galaxies; asterisks are lobe-dominated quasars and stars are core-dominated quasars. When 1σ error bars are not visible they are smaller than symbols. Axis are the logarithm of the defined quantity.

Absorbed X-ray emission in radio-quiet AGN is associated with the power of the central engine. We thus also tested possible relations between the high-energy X-ray emission from the core and the large-scale radio emission, which should be an indicator of the overall power emitted over the source life-time. This is shown in Figure 3, where the 2-10 keV luminosity (assuming isotropic emission) is plotted versus the 178 MHz luminosity density (K -corrected adopting the value of α_R specific to each source as listed in Table 6). For radio galaxies we measured the high energy luminosity of the absorbed component. We observe a large dispersion in these two values, showing that if any correlation exists, it is weak.

We notice that radio galaxies lie below quasars in this plot. This is an additional indication that the X-ray emission is relativistically boosted, and the values for the quasars are higher than those for radio galaxies due to beaming in the line of sight. On the other hand, the lack of correlation between these two parameters may also be an indication that absorbed emission from radio galaxies is at least in part jet-related.

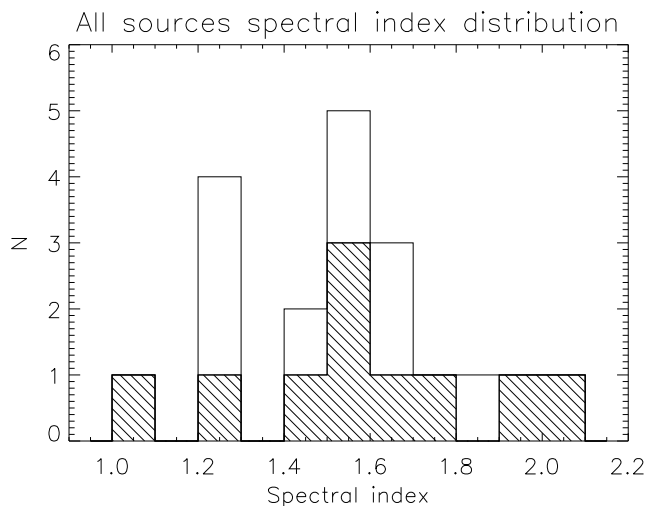
5.3 Spectral index distribution

Figure 4 shows the distribution of the spectral index for the whole sample. For radio galaxies this is the spectral index of the absorbed component. The histogram shows that the population of radio galaxies and quasars have a similar spectral index distribution. A Kolmogorov-Smirnov (K-S) test applied to the two populations does not allow us to reject the null hypothesis that the two groups of data are drawn from the same distribution (the probability of obtaining a K-S statistic equal to or more extreme than the one observed is $p = 0.828$). We calculated mean, median and a bi-square weighted mean for the whole sample and each subsample (see Table 8). In addition to the classical mean value we calculated a more robust mean using the method described in Worrall (1989), which takes into account the errors associated with each data point and fits an intrinsic dispersion in spectral index. Bearing in mind that the samples are small, the different estimates of the mean values are in agreement.

³ <http://www.3crr.dyndns.org/cgi/database>

Table 7. Correlation results of linear regression for logarithmic luminosity-luminosity relations. Small Z -values mean the correlation is less significant.

Subsample	Number	Kendall's τ Z-value	Probability	Intercept	Slope	Dispersion
All sources	19	4.42	0.00001	$6.3^{+1.4}_{-4.1}$	$0.63^{+0.15}_{-0.06}$	0.38
Core-dominated QSO	4	1.08	0.2786	$0.4^{+9.0}_{-9.0}$	$0.84^{+0.30}_{-0.30}$	0.04
Radio galaxies	10	2.06	0.0397	$-4.6^{+7.0}_{-10.0}$	$1.07^{+0.4}_{-0.4}$	0.57
Core-dominated QSO and radio galaxies	14	3.62	0.0003	$5.0^{+1.9}_{-4.5}$	$0.68^{+0.12}_{-0.08}$	0.43


Figure 4. Spectral index distribution for the whole sample. The dashed histogram illustrates the distribution of the absorbed components of radio galaxies, and empty boxes represent quasars.

The maximum-likelihood analysis gives a mean spectral index for the whole sample of 1.55 ± 0.17 . Radio galaxies and lobe-dominated quasars have mean value of $\Gamma = 1.57$ and $\Gamma = 1.59$, respectively, and the core-dominated quasar subsample has a mean value of $\Gamma = 1.45$, significantly different from the other two populations (see Table 8).

We find a different behaviour when looking at the unabsorbed, soft power law characterising some of the radio galaxies in the sample. For the four radio galaxies for which a spectral index was determined, we find a mean spectral index $\Gamma_{ML} = 2.05 \pm 0.25$. Although errors are large, this analysis suggests that when an unabsorbed soft component is present, its spectrum is relatively steep. A K-S test applied to the spectral index of the unabsorbed components of radio galaxies and the absorbed components of the whole sample allows us to reject the null hypothesis that the two samples are drawn from the same population at better than 99 per cent confidence.

6 DISCUSSION

We have assembled X-ray results for a sample of 19 radio galaxies (RGs) and radio-loud quasars (RLQs) for which core spectral properties have been derived with good precision. Core spectral properties have been discussed before for RLQs at high redshift

(e. g., Brinkmann, Yuan & Siebert 1997; Brinkmann et al. 2000; Reeves & Turner 2000; Brunetti et al. 2002; Hardcastle et al. 2002; Hasenkopf, Sambruna & Eracleous 2002; Donahue et al. 2003; Belsole et al. 2004; Galbiati et al. 2005), in particular for core-dominated sources with resolved jet-emission (e.g. Tavecchio et al. 2002; Gambill et al. 2003; Marshall et al. 2005).

This is the first time that the unabsorbed and absorbed X-ray emission from RGs at $0.5 < z < 1.0$ has been measured with precision in a systematic way and with a well-defined sample. Previous large-scale analyses of the X-ray spectrum of RGs have been limited to the soft (unabsorbed) X-ray emission from these sources and/or have had insufficient spatial or spectral resolution to allow separation of core and extended emission.

Our sample allows us to discuss our spectral results in the context of unification schemes.

6.1 The origin of the core X-ray emission

The *Chandra* spatial resolution allows us to separate emission from the core and to establish, through spectral fitting, that the emission from the central 5 pixels of the observation for 17 of the 18 sources in the sample can be described by one or more power laws. 3C 292, observed only with *XMM-Newton*, also shows power-law emission in the core spectrum. The nuclear X-ray continuum is well described by a single power law with Galactic absorption for all quasars, while 70 per cent of RGs in our sample show intrinsic absorption ranging from 0.3 to $50 \times 10^{22} \text{ cm}^{-2}$. For about 50 per cent of all sources, mostly RGs, we conclude that a single power-law model does not satisfactorily fit the data.

As discussed in the introduction, the soft X-ray nuclear emission of core-dominated quasars is consistent with that arising from a relativistic jet, in agreement with results based on data from *Einstein* (e.g. Shastri et al. 1993), *ROSAT* (e.g., Brinkmann, Yuan & Siebert 1997; Hardcastle & Worrall 1999), and *ASCA* (e.g. Reeves & Turner 2000). Only very few radio galaxies have been detected with *ROSAT* at soft energy, and they were found to lie on an extension of the flux-flux correlation for core-dominated quasars (Worrall et al. 1994; Hardcastle & Worrall 1999). We follow the interpretation of Worrall et al. (1994) in explaining the lower X-ray flux density of the radio galaxies as due to the effect of a relativistic jet which beams the emission from the core-dominated quasars into the line of sight.

Our study shows that radio-galaxy soft X-ray flux density is indeed consistent with being unboosted emission from the same component as seen in the core-dominated quasars (Fig. 2). However, the spectrum is significantly steeper, with an average value of $\Gamma \sim 2.1$ ($\alpha \sim 1.1$), and is consistent with the extrapo-

Table 8. Average value of spectral index. For radio galaxies both absorbed and unabsorbed components are tabulated. Col. 1: subsample under analysis; Col. 2.: number of objects in the subsample; Col. 3: Mean value and standard deviation; Col. 4: median value and associated error; Col. 5: bi-square weighted mean and robust error estimate; Col. 6: Maximum-likelihood method mean and error.

Subsample	Number	Mean	Median	BW-mean	ML-mean
All sources	19	1.54±0.19	1.54±0.19	1.54±0.27	1.55 ^{+0.05} _{-0.04}
Absorbed PL Radio Galaxies	10	1.56±0.21	1.59±0.21	1.56±0.32	1.57 ^{+0.03} _{-0.02}
Core-dominated QSO	4	1.40 ± 0.14	1.54 ± 0.14	1.40±0.17	1.45 ^{+0.06} _{-0.06}
Lobe-dominated QSO	5	1.60±0.19	1.65±0.18	1.60±0.26	1.59 ^{+0.09} _{-0.09}
All QSO	9	1.51±0.18	1.54±0.17	1.51±0.23	1.52 ^{+0.06} _{-0.07}
Unabsorbed PL Radio Galaxies	4 ^a	2.15±0.28	2.10±0.25	2.13±0.40	2.05 ^{+0.24} _{-0.25}

^a Statistical analysis is performed using only those sources with detections.

lation of a broken-power law synchrotron spectrum of $\Delta\alpha \sim 0.5 - 0.9$ from radio frequencies, as observed in the resolved jets of lower-redshift FRI radio galaxies (e.g. Böhringer et al. 2001, Hardcastle, Birkinshaw & Worrall 2001; Worrall et al. 2001b). The steep spectrum disfavours inverse Compton (IC) scattering as the mechanism for *this* emission. On the other hand, the flat X-ray spectrum ($\alpha \sim 0.45$) observed in core-dominated quasars is suggestive of IC emission becoming dominant as the Doppler factor becomes larger (e.g., Kembhavi, Feigelson & Singh 1986). In core-dominated quasars the inner jet is unobscured, and synchrotron self-Compton emission and upscattering of external photons from the nucleus are expected to dominate, while scattering of cosmic microwave background (CMB) photons by a beamed jet might become important at larger jet radii. Since increased beaming depresses the X-ray to radio (IC to synchrotron) ratio, the slope of the correlation in Figure 2 (1.0 for radio galaxies, flattening to 0.8 for core-dominated quasars) can be qualitatively understood, and confirm previous work within the limited statistics of our sample of core-dominated quasars.

The biggest surprise is that, with the exception of 3C 292 and 3C 330, the absorbed components of radio galaxies have flatter spectra ($\Gamma = 1.57^{+0.03}_{-0.02}$) than those of radio-quiet quasars (RQs) (typically $\Gamma \sim 1.9-2.0$, e.g. Yuan et al. 1998; Reeves & Turner 2000) and consistent with the best-fitting power law of RLQs ($\Gamma = 1.52^{+0.06}_{-0.07}$), although somewhat steeper than the core-dominated sample alone ($\Gamma = 1.45 \pm 0.06$).

There are two possible explanations for this observation. One is that the X-ray properties of the accretion regions in radio-loud and radio-quiet objects are different. However, if we wish to retain a simple unification scheme in which radio-loud sources are essentially radio-quiet ones with the addition of jets, then our results imply that the absorbed emission that we measure in 70 per cent of the RGs in our sample is primarily associated with the inner jet rather than with the accretion region. There is no reason in principle why jet emission cannot come from within the torus, and the flat X-ray spectrum of this emission is certainly consistent with a jet model.

It is thus interesting to ask whether the central engine is the same in radio-loud and radio-quiet objects. For lobe or core-dominated quasars the beamed and unbeamed components cannot be separated, but radio galaxies allow us to try to answer this ques-

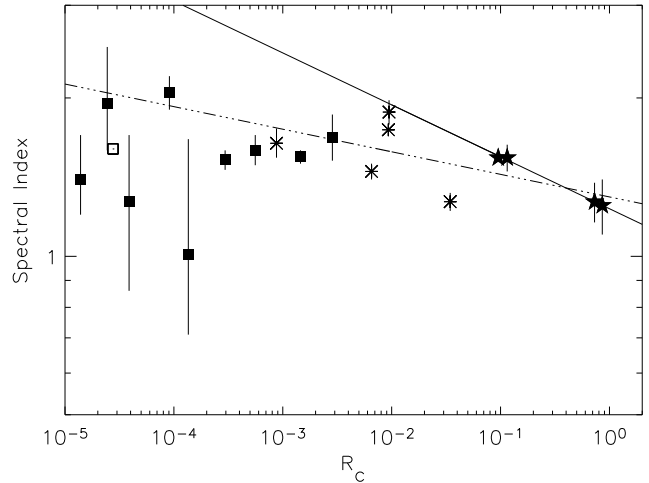


Figure 5. X-ray spectral index (absorbed component for radio galaxies) versus the radio core prominence parameter R_C . Symbols are as in Fig. 2, the white box is 3C 427.1 for which the spectral index was fixed. The dot-dashed line is the best-fit Buckley-James (B-J) correlation (as implemented in ASURV Rev 1.1 and presented in Isobe, Feigelson & Nelson (1986)) to the subsample of quasars; the continuous line is the best-fit B-J regression to the subsample of core-dominated quasars.

tion. We can ask at what level absorbed emission with a steep spectrum as measured for RLQs may be present in radio galaxies, assuming that we are not sensitive enough to measure it. If a steep component of high absorption is mixed with a flatter one with lower absorption then the fitted slope can be relatively flat and unabsorbed, even if the absorption-corrected luminosity of the steeper component is significant.

The result shown in Figure 3, in which radio-galaxy X-ray luminosities are lower than those of quasars, may support this. Although we expect core-dominated quasars to have higher luminosities, since no correction for beaming is applied, this may also suggest that part of the difference between the two populations of sources arises because radio-galaxy luminosities are underestimated if the correct model has an additional steep absorbed component of high intrinsic luminosity.

Further support comes from Figure 5. Here the spectral in-

dex (absorbed component for radio galaxies) is plotted versus the core-dominance parameter R_c . This is defined as the ratio between the core luminosity density at 5 GHz and the large scale luminosity density at 178 MHz ($R_c = L_{5\text{GHz}}/L_{178\text{MHz}}$) and is accepted as an orientation parameter. In agreement with what has been found earlier with larger samples (e.g., Kembhavi, Feigelson & Singh 1986; Brinkmann, Yuan & Siebert 1997), at least for core- and lobe-dominated quasars, we observe a tendency for the spectral index Γ to increase with lower core dominance. However, no information was available in these earlier studies on the absorbed components of RGs. The sample of RGs discussed here extends the sampling of the core-dominance parameter by 2 order of magnitude over the use of quasars alone. The anti-correlation for core-dominated quasars is significant at the 90 per cent level on a Kendall's τ test. The anti-correlation is also valid for the population of all quasars (lobe-dominated plus core-dominated), but the slope tends to zero, the smaller R_c becomes.

This result could be an indication of the presence of an additional, *isotropic* spectral component in the radio-galaxy population. We may be indirectly observing the effects of accretion-related emission similar to that observed in RQQs, i.e. heavily absorbed and with spectral slope ~ 2 , which may be (partially) masked by a less absorbed, jet-related component.

In an attempt to test this hypothesis quantitatively for the RGs in our sample, we simulated a spectrum in XSPEC using the response file for the core region of one of the radio galaxies. We initially simulated a power law of spectral index $\Gamma^{\text{steep}} = 1.9$, which is similar to that found for RQQs (e.g. Reeves & Turner 2000) absorbed by a column density $N_{\text{H}}^{\text{steep}} = 10^{24} \text{ cm}^{-2}$, i.e. \sim a factor of ~ 10 higher than the average absorption found for radio galaxies of our sample. We then added a flatter power law (of $\Gamma^{\text{flat}} = 1.57$, the average value for radio galaxies; see Table 8) absorbed by a column density $N_{\text{H}}^{\text{flat}} = 10^{23}$. For simplicity we ignored a soft unabsorbed component. We varied the normalization of the steeper power law until the whole spectrum was fitted with a single power law. We found that with a large number of counts (excellent photon statistics) the steep power law is washed out if its contribution to the normalization at 1 keV is < 10 per cent of the softer power law.

The statistics in real observations are limited by effective area and exposure time. We thus repeated the same exercise using photon statistics similar to those of our data. This yielded the conclusion that a steep, absorbed power law is not detected spectrally in the presence of a flatter and less absorbed power law emission if the 1-keV normalizations of the two components are similar.

If the normalization at 1 keV of the steeper highly absorbed power law is a factor of two greater than the original less absorbed component, then we still find that the whole spectrum can be fitted with a single power law of a spectral index which is found to be flatter than Γ^{flat} . This may explain, for example, the very flat absorbed-power-law slope of 3C 265. The result can be attributed to the ACIS-S response: since the sensitivity at 1 keV is higher than at higher energies, the effect of the flat spectrum resulting from the large absorption dominates that of the steep spectrum at high energy.

A steep-spectrum core-related component of intrinsic luminosity at least a factor of two greater than the 2–10 keV luminosity that we actually measure may be present for all our absorbed radio galaxies, and with the current data we are unable to separate this component. Our simulations thus support the hypothesis that the observed absorbed emission from RGs is jet-related or jet-dominated. However we cannot exclude the possibility that the central AGN in RLQs and RQQs are different.

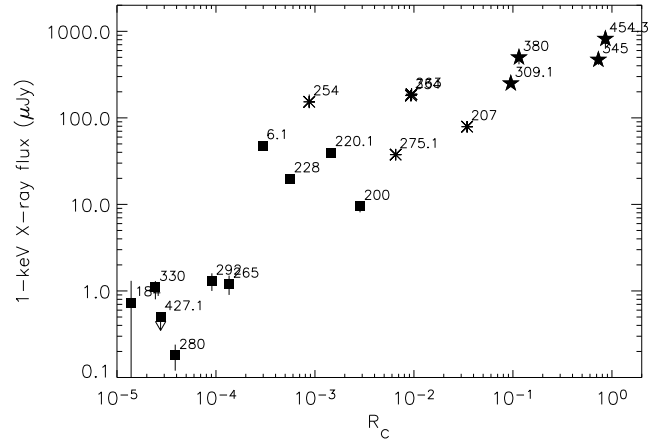


Figure 6. X-ray flux density versus the radio core prominence parameter R_c . The 3CRR designation for each galaxy is also marked. Symbols are as in Fig. 2.

6.2 The effect of orientation and implications for unification schemes

The correlation between the X-ray flux density at 1 keV and the core prominence parameter R_c (Fig. 6) is an alternative representation of information shown in Figure 2, since the sources have similar isotropic luminosities and the 5-GHz flux density is beamed. However, we notice that the RGs with no or weak absorption are those with a larger R_c and that they occupy a position in that plot which is closer to that of lobe-dominated quasars. This is consistent with the expectations from unified models, in which the X-ray emission from quasars which are viewed at a large angle to the line of sight is the sum of jet-related and core-related emission.

The finding that only RGs show intrinsic, rest-frame absorption is again in agreement with unification models if these sources are viewed in the plane of the sky through an absorber. If emission from RGs is not affected by beaming, we expect a slope close to 1 for the correlation between X-ray and radio core emissions, which is what we find. Moreover, we also find that the slope of the correlation valid for radio and X-ray flux density becomes smaller the more the beaming is expected to play a role, as in core-dominated quasars (but note that this effect is less observed in the luminosity-luminosity relations). This is an indirect indication of the different effects of beaming in the X-ray and the radio, which depends on the mechanism responsible for the emission. We argued in Sec. 6.1 that it is likely that synchrotron radiation accounts for the jet X-ray emission in radio galaxies and that IC becomes important, or even dominant, in core-dominated quasars.

We do not find any correlation between the absorption and the redshift, as found for larger samples of both RQQs and RLQs (e.g. Reeves & Turner 2000; but the correlation is significant only for sources at redshift above 1), but we notice that the 3 RGs in our sample which do not show intrinsic absorption are also those at lower redshift. No significant correlation was found between the intrinsic N_{H} and the spectral index, strengthening the constraints we can put on these two parameters, since they are intrinsically correlated.

A new result is that the unabsorbed non-thermal emission from RGs is consistent with synchrotron emission from a high-energy extension of the electrons which emit at radio frequencies. Because of the relatively short energy-loss timescales of the responsible electrons we may expect soft X-ray variations on short

timescales for at least some of these sources. This is not observed, but this may be an effect of the limited statistics available for such high redshift objects.

7 SUMMARY AND CONCLUSIONS

We have presented X-ray spectra of the unresolved components of 9 quasars and 10 radio galaxies which were similar in isotropic radio power and which lie in the redshift range $0.5 < z < 1.0$. This is the first time that two spectral components have been reported in the core spectra of a reasonably large sample of radio galaxies. We have compared our results with the expectations from a unification model that describes each source as having a) a central largely isotropic X-ray component similar to the X-ray core of a radio quiet quasar; b) a torus that absorbs X-ray core emission from sources whose jets are in the plane of the sky (namely radio galaxies), and c) X-ray jet emission on scales comparable with and larger than the torus

Several results support this simple unification model and allow conclusions to be drawn about the origin of the X-ray emission in both radio galaxies and quasars:

(i) Radio galaxies display higher intrinsic absorption than quasars, as expected from b);

(ii) An unabsorbed X-ray component is also seen in radio galaxies; we interpret this component as arising from the jet. Its steep slope (steeper than the radio spectrum) is consistent with a synchrotron origin;

(iii) Radio galaxies show a radio-core/X-ray-core correlation of slope ≈ 1 when the unabsorbed X-ray component is used. This also argues in favour of a jet-related emission.

(iv) The radio-core/X-ray-core correlation flattens when quasars are considered, i.e. they are relatively X-ray under-luminous for a given radio flux density. This is qualitatively consistent with IC X-ray emission becoming more dominant than synchrotron in the jet as the angle to the line of sight is decreased and beaming becomes more important. The flat X-ray slope of the core-dominated quasars (similar to the radio slope) supports this conclusion. Beaming causes the jet to outshine other core components in the X-ray.

(v) The lobe-dominated quasars have somewhat more X-ray emission than expected on the basis of the jet component in radio galaxies, implying an unabsorbed contribution from the inner nucleus that is not outshone by beamed emission in these sources. The two contributions to the X-ray emission cannot be separated with current statistics.

(vi) Although the radio galaxies show absorbed X-ray emission, its spectrum is flatter than is typically seen in RQQs. This implies that either the nuclear emission is affected by the presence of a jet or that the absorbed emission is largely from the jet. We have shown through simulations that it is possible that a steep-spectrum absorbed core can be present, but masked by jet emission.

ACKNOWLEDGEMENTS

E.B. thanks PPARC for support and MJH thanks the Royal Society for a research fellowship. We are grateful to D. A. Evans for long and helpful discussions about pileup, and thank G.W. Pratt for a careful reading of the manuscript. E. B. thanks M. Cappi for interesting discussion. We acknowledge an anonymous referee for helpful comments and suggestions which improved the manuscript.

This research has made use of the the SIMBAD database, operated at CDS, Strasbourg, France, and the NASA/IPAC Extragalactic Database (NED) which is operated by the Jet Propulsion Laboratory, California Institute of Technology, under contract with the National Aeronautics and Space Administration.

REFERENCES

- Aller M. F., Aller H. D., Hughes P. A., 2003, *ApJ*, 586, 33
 Ballet J., 1999, *A&AS*, 135, 371
 Barthel P.D., 1989, *ApJ*, 336, 606
 Belsole E., Worrall D. M., Hardcastle M. J., Birkinshaw M., Lawrence C. R., 2004, *MNRAS*, 352, 924
 Böhringer H., Belsole E., Kennea J., et al., 2001, *A&A*, 365, L181
 Bondi M., Brunetti G., Comastri A., Setti G., 2004, *MNRAS*, 354, 43
 Bridle, A.H. & Fomalont, E.B., 1978, *AJ*, 83, 704
 Brinkmann W., Laurent-Muehleisen S. A., Voges W., Siebert J., Becker R. H., Brotherton M. S., White R. L., Gregg M. D., 2000, *A&A*, 356, 445
 Brinkmann W., Yuan W., Siebert J., 1997, *A&A*, 319, 413
 Brunetti G., Bondi M., Comastri A., Setti G., 2002, *A&A*, 381, 795
 Canizares C.R., White J.L., 1989, *ApJ*, 339, 27
 Crawford C.S., Fabian A.C., 2003, *MNRAS*, 339, 1163
 Croston J.H., Hardcastle M.J., Harris D. E., Belsole E., Birkinshaw M., Worrall D.M., 2005, *ApJ*, 626, 733
 Davis J.E., 2001, *ApJ*, 562, 575; <http://space.mit.edu/%7Edavis/papers/pileup2001.ps>
 Dickey J.M. & Lockman F.J., 1990, *ARA&A*, 28, 215
 Donahue M., Daly R. A., Horner D. J., 2003, *ApJ*, 584, 643
 Evans D.A., Hardcastle M.J., Croston J.H., Worrall D.M., Birkinshaw M., 2005, *MNRAS*, 359, 363
 Galbiati E., et al., 2005, *A&A*, 430, 927
 Gambill J.K., Sambruna R.M., Chartas G., Cheung C. C., Maraschi L., Tavecchio F., Urry C.M., Pesce J.E., *A&A*, 401, 505
 Hardcastle M. J., Worrall D. M., 1999, *MNRAS*, 309, 969
 Hardcastle M.J., Worrall D. M., 2000, *MNRAS*, 319, 562
 Hardcastle M. J., Birkinshaw M., Worrall D. M., *MNRAS*, 326, 1499
 Hardcastle M.J., Birkinshaw M., Cameron R. A., Harris D. E., Looney L. W., Worrall D. M., 2002, *ApJ*, 581, 948
 Hardcastle M. J., Harris D. E., Worrall D. M., Birkinshaw M., 2004, *ApJ*, 612, 729
 Hasenkopf C.A., Sambruna R.M., Eracleous M., 2002, *ApJ*, 575, 127
 Heckman T.M., Chambers K.C., Postman M., 1992, *ApJ*, 391, 39
 Hes R., Barthel P.D., Hoekstra H., 1995, *A&A*, 303, 8
 Hough D. H., Vermeulen R. C., Readhead A. C. S., Cross L. L., Barth E. L., Yu L. H., Beyer P. J., Phifer E. M., 2002, *AJ*, 123, 125
 Kembhavi A., Feigelson E.D., Singh K.P., 1986, *MNRAS*, 220, 51
 Isobe T., Feigelson E. D., Nelson P. I., 1986, *ApJ*, 306, 490
 Isobe T., Feigelson E.D., Akritas M. J., Babu J., 1990, *ApJ*, 346, 104
 Laing R. A., Riley J. M., Longair M. S., 1983, *MNRAS*, 204, 151
 LaValley M., Isobe T., Feigelson E. D., 1992, *BAAS*, 24, 839
 Lister M. L., Tingay S. J., Preston R. A., 2001, *ApJ*, 554, 964
 Marshall H.L., et al., 2005, *ApJS*, 156, 13

- McCarthy P. J., van Breugel W., Spinrad H., Djorgovski S., 1987, *ApJ*, 321, 29
- Meisenheimer K., Haas M., Müller S. A. H., Chini R., Klaas U., Lemke, D., 2001, *A&A*, 372, 719
- Prieto M. A., 1996, *MNRAS*, 282, 421
- Ridgway S. E., Stockton A., Lacy M., 2004, *ApJ*, 600, 70
- Reeves J.N., Turner M.J.L., Ohashi T., Kii T., 1997, *MNRAS*, 292, 468
- Reeves J.N., Turner M.J.L., 2000, *MNRAS*, 316, 234
- Sambruna R. M., Eracleous M., Mushotzky R. F., 1999, *ApJ*, 526, 60
- Shastri P., Wilkes B. J., Elvis M., McDowell, J., 1993, *ApJ*, 410, 29
- Shi Y., et al., 2005, *ApJ*, in press (astro-ph/0504622)
- Tavecchio F., et al., 2002, *ApJ*, 575, 137
- Unwin S. C., Wehrle A. E., Lobanov A. P., Zensus J. A., Madejski G. M., Aller M. F., Aller, H. D., 1997, *ApJ*, 480, 596
- Urry C.M., Padovani P., 1995, *PASP*, 107, 803
- Yuan W., Brinkmann W., Siebert J., Voges W., 1998, *A&A*, 330, 108
- Worrall D. M., 1989, in *AGN and the X-ray Background*, Proceedings of the 23rd ESLAB Symposium, Bologna, ESA SP-296, p. 719-726.
- Worrall D.M., Wilkes B.J., 1990, *ApJ*, 360, 396
- Worrall D.M., Lawrence C. R., Pearson T. J., Readhead A. C. S., 1994, *ApJ*, 420, 17
- Worrall D. M., Birkinshaw M., Hardcastle M. J., Lawrence C. R., 2001a, *MNRAS*, 326, 1127
- Worrall D.M., Birkinshaw M., Hardcastle M.J., 2001b, *MNRAS*, 326, L7

APPENDIX A: NOTES ON PARTICULAR SOURCES AND COMPARISONS WITH THE LITERATURE

3C 6.1: the source was observed in two separate exposures of 36 ks (Obs ID 3009) and 20 ks (Obs ID 4363), respectively. We extracted the spectrum in the same region (a circle of radius 2.5 pixels) for the two exposures. Observation 3009 contains 1568 net counts in the 0.2-10.0 keV energy band. Observation 4363 contains 758 counts in the same energy band. The two spectra were fitted simultaneously. We fitted the spectrum with a model composed of a power law and a pileup model. However the addition of the pileup model does not improve the fit, and in each exposure the estimated PUF is less than 8 per cent. X-ray emission is also observed from hotspots (Hardcastle et al. 2004) and from the lobes (Croston et al. 2005). With a mean flux of 0.044 ± 0.008 for Obs ID 3009 and of 0.039 ± 0.014 for Obs ID 4363, no significant variability can be claimed.

3C 184: the *Chandra* data do not contain enough counts (15 ± 4 net counts) to perform a spectral analysis. For this source the spectral properties of the core are derived from *XMM-Newton* data. The source is very small in the radio, with a maximum extent of only 5 arcsec. As discussed in Belsole et al. (2004) the *XMM-Newton* spectrum is fitted by a three-component model representing the emission from a cluster-like atmosphere, with best-fit parameters $kT = 3.6_{-1.8}^{+10.6}$ keV, $Z/Z_{\odot} = 0.3$, and bolometric $L_X = 1.1 \times 10^{44}$ erg s^{-1} ; a jet/lobe related soft non-thermal component; and a core-related absorbed power law component as listed in Table 4.

3C 200: the source shows extended X-ray emission out to 10 arcsec, but point-like emission dominates within the 2.5 pixel radius of the circle used for the core spectral analysis. The X-ray properties of

the core of this source have not been described previously in the literature.

3C 207: the core spectrum of 3C 207 is best-fitted with a single power-law of rather flat slope $\Gamma = 1.27 \pm 0.05$. This is in agreement with what was found previously by Brunetti et al. (2002) ($\Gamma = 1.22 \pm 0.06$), and Gambill et al. (2003) ($\Gamma = 1.36 \pm 0.06$). We do not find evidence for absorption above the Galactic value as found by Brunetti et al. (2002), and, although we do not exclude emission of ionized gas in the nucleus, the addition of a Gaussian iron line does not improve the fit statistically. Hotspot, jet, lobe and extended emission were also previously discussed (e.g., Brunetti et al. 2002, Hardcastle et al. 2004, Gambill et al. 2003). The 2.0–10.0-keV flux we found is somewhat lower than found by Gambill et al. (2003), but the two values agree within 20 per cent.

3C 220.1: the source shows extended emission which is likely to be cluster-like in origin (Worrall et al. 2001a). The spectral index we found is somewhat flatter than that found by Worrall et al. (2001a), who found that intrinsic absorption was required. When our results are compared with the Worrall et al. fit without intrinsic absorption then the two slopes are in good agreement. Moreover, after taking into account the different cosmological parameters, fluxes and luminosities are in agreement.

3C 228: the source was observed in two separate exposures of 10 ks (Obs ID 2453) and 13 ks (Obs ID 2095), respectively, after flare screening. The shorter observation detected 281 net counts, while the longer has 365, consistent with no flux variation between the two.

3C 254: the source is piled up. Within uncertainties our power-law slope is in agreement with that found by Donahue et al. (2003) using the same data. The flux and luminosity are also in agreement after considering the different cosmological parameters. The 1-keV flux density is 1/3 greater than that found by Hardcastle & Worrall (1999), but this is likely to be within the large uncertainties arising from the *ROSAT* analysis.

3C 263: the source is heavily piled up. We examined the spectrum extracted in several regions and we finally adopted the annular region of inner radius 3 pixels and outer radius 5 pixels as the least affected by pileup. The background spectrum was extracted in an annulus of inner and outer radii 9 and 12 pixels, respectively. We also excluded the emission from the jet using a rectangular region. The power-law slope agrees with that found by Hardcastle et al. (2002) using the same data to within 1σ errors. The 1-keV flux density differs significantly, with our value found to be 50 per cent lower, even after according a systematic error of 10 per cent to account for the PSF correction factor. This is likely to be due to a combination of a different region used (Hardcastle et al. used a circle of radius 5 pixels) and improvement in the calibration since the Hardcastle et al. analysis, or their use of a pileup model rather than fitting the spectrum in an annulus.

3C 265: the fit of this source spectrum requires 5 components. The model is composed of Galactic absorption, a power law, an absorbed power law and a Gaussian at the energy of the neutral iron line. Bondi et al. (2004) discussed the properties of this source in detail. We find that the slope of the absorbed power law is consistent with the result of Bondi et al. (2004).

3C 275.1: there is no evidence for X-ray emission from a resolved jet, but the source shows extended emission which has been interpreted as arising from a cluster-like atmosphere (Crawford & Fabian 2003; Hardcastle & Worrall 2000) or from lobe inverse-Compton emission (Croston et al. 2005).

3C 280: this source is one of the best studied powerful radio galaxies. It has an extended emission-line (OII) nebula with a

central peak and a loop around the eastern radio lobes (e.g., McCarthy et al. 1987; Ridgway, Stockton & Lacy 2004). We selected a background in the canonical annulus of inner radius 3.5 pixels and outer radius 6 pixels, but we also excluded the eastern and western regions corresponding to the X-ray lobes. There are only 50 net source counts, but these are at energies above 1 keV, suggesting that we are seeing an absorbed power law. Donahue et al. (2003), also using *Chandra* data, find a very flat spectral index, consistent with zero, when fitting between 0.3 and 8.0 keV. The 1-keV flux density we found is in agreement with their result. 3C 280 was one of the few high-redshift radio galaxies with a clear *ROSAT* detection (Worrall et al. 1994). Discrepancies between the *ROSAT* and *Chandra* results have been discussed by Donahue et al. (2003).

Constraints on the soft emission were obtained by fixing the slope of the unabsorbed power law to 2.1, as for other radio galaxies for which direct fitting was possible. The absorbed component parameters were also fixed to obtain constraints on the normalization of the unabsorbed component. Because parameter values have been fixed, we added a systematic error of 20 per cent to the flux and luminosity of the unabsorbed component.

3C 292: we used *XMM-Newton* data for this source. Details of the analysis are described by Belsole et al. (2004). The core spectrum extracted in a circle of radius 10 arcsec was fitted with a two-power-law model. The source also shows extended X-ray emission coincident with the radio lobes but little spectral evidence for a cluster-like atmosphere.

3C 309.1: our estimate of the X-ray flux density at 1 keV is in very good agreement with previous results from *ROSAT* observations (Hardcastle & Worrall 1999).

3C 330: the source X-ray image shows the presence of some extended emission aligned with the radio lobes (see also Croston et al. 2005; Hardcastle et al. 2002). Core emission was analysed previously using *Chandra* data (Hardcastle et al. 2002) and results are in good agreement despite the slightly different regions used for spectral analysis.

3C 334: a reduced χ^2 of 1.35 suggests that an additional component may be necessary. However, the addition of a thermal or power-law component does not improve the fit. Some residuals are observed at low energy (below 0.7 keV) suggesting a soft excess.

3C 345: in agreement with Gambill et al. (2003) we find that two power laws are necessary to fit the spectrum from this source: a steeper ($\Gamma = 1.8$) slope fits the soft spectrum, while a flatter ($\Gamma \sim 1.3$) is used to represent that hard spectrum. Using the broken-power-law model we find an energy break of 1.74 ± 0.33 keV, in agreement within the errors with Gambill et al. (2003).

3C 380: the strong pileup for this source led us to mask a central circle of radius 1.5 arcsec. Our result is in agreement with that found by Prieto (1996) using *ROSAT* data ($\Gamma = 1.58 \pm 0.13$) and consistent with the photon index recently published by Marshall et al. (2005): $\Gamma = 1.61 \pm 0.09$. However there is a discrepancy between our and their measure of the X-ray flux. We and Marshall et al. (2005) extracted the spectrum from the same area; we used slightly different background, but the background is negligible for such a high-flux source. However, the big difference between the two studies is the calibration. Our newer analysis has taken into account the charge transfer inefficiency and the ARF is better determined. Moreover, without using a pileup model, Marshall et al. found a poor fit, with a spectrum that was inconsistently flatter than that in the current work, and consequently a lower 1-keV flux density. Marshall et al. attributed the flat spectrum and bad fit to pileup, but

the improved calibration now available allows a more precise flux density to be determined.

3C 427.1: the statistics are not sufficient to perform conclusive spectral fitting. The spectrum is dominated by hard emission, with only 3 of the 15 counts found at energy below 2 keV. We fixed the parameters for an absorbed power law to typical values found for the other radio galaxies in the sample. We thus adopted a model composed of an absorbed power law of spectral index 1.6, and intrinsic absorption $1 \times 10^{23} \text{ cm}^{-2}$. We also obtained an upper limit for the presence of an unabsorbed soft component.

3C 454.3: the source is heavily piled up. We extracted the spectrum in an annulus of inner and outer radii 2.0 and 2.5 pixels. Although in this region any effect of pileup is negligible (and indeed the addition of a pileup model does not improve the fit), the best-fit spectral index is rather flat. Marshall et al. (2005) found a slightly steeper spectral index, but this is attributable to the different calibration used (see also 3C 380). As in the case of 3C 380, when the spectrum is fitted above 1 keV the two results are in better agreement. Our best-fit Γ is also in agreement with Tavecchio et al. (2002) who used *BeppoSAX* data. Discrepancy in the 1-keV flux quoted by us and Marshall et al. are explicable as for the case of 3C 380.